Corrosion Science 195 (2022) 110007

Contents lists available at ScienceDirect

Corrosion Science

journal homepage: www.elsevier.com/locate/corsci

Hydrogen embrittlement of additively manufactured $AlCoCrFeNi_{2.1}$ eutectic high-entropy alloy

Di Wan [a,*], Shuai Guan [b], Dong Wang [a], Xu Lu [a], Jun Ma [a]

[a] Department of Mechanical and Industrial Engineering, Norwegian University of Science and Technology, Richard Birkelands vei 2B, 7491 Trondheim, Norway
[b] Advanced Manufacturing Technology Research Center, Department of Industrial and Systems Engineering, The Hong Kong Polytechnic University, Hung Hom, Kowloon, Hong Kong

ARTICLE INFO

Keywords:
High-entropy alloy (HEA)
Tensile test
Hydrogen embrittlement
Additive manufacturing
Electron backscattered diffraction (EBSD)
Electron channeling contrast imaging (ECCI)

ABSTRACT

$AlCoCrFeNi_{2.1}$ eutectic high-entropy alloy (HEA) was fabricated in as-cast and additively manufactured (AM) states. The hydrogen embrittlement susceptibility of both materials was investigated through in-situ uniaxial tensile test. Combining several advanced high-resolution scanning electron microscopy (SEM)-based techniques, the deformation and hydrogen embrittlement behavior have been intensively discussed. Interfacial cracking along both phase boundaries and grain boundaries are found to be responsible for the hydrogen-assisted fracture of this material. The cracking susceptibility has a dependence on the manufactured phase morphology. The orientation relationship between the phases and the misorientation between grains also have a significant impact on the hydrogen-induced cracks.

1. Introduction

High-entropy alloys (HEAs) comprise multiple principal elements, with the concentration of each element between 5 and 35 at% [1]. Such a novel alloy design approach has resulted in several HEA systems with extraordinary properties, such as high fracture toughness at cryogenic temperatures [2], high strength at elevated temperatures [3] and excellent resistance to corrosion [4], indicating the promising potentials of the HEAs for harsh environments applications. HEAs typically crystallize as face-centered cubic (FCC), body-centered cubic (BCC) or hexagonal close packed (HCP) solid solution phases, due to their high configuration entropy and hence the low Gibbs free energy that suppress the formation of intermetallic phases [5–9]. As one of the most popular FCC HEAs, the equiatomic CrMnFeCoNi alloy in the as-cast or wrought-annealed states deforms via both dislocation motions and nano-twinning during tensile straining, which maintains the substantial and sustained strain hardening rate and hence leads to the excellent ductility [2,5]. However, the tensile yield strength of FCC HEAs is often insufficient. In contrast, BCC HEAs, often comprising large amounts of refractory BCC metals as principal elements (e.g. W, Mo, Nb, Ta and V), can maintain a very high strength over a wide range of temperatures, with significant sacrifice of ductility [10]. Deviating from those single-phase FCC or BCC HEAs, the eutectic HEAs provide the probability of achieving both hard and soft phases and hence the enhanced strength-ductility synergy [11]. Till to date, several eutectic HEAs have been designed, including $AlCoCrFeNi_{2.1}$ [12,13], $AlCrFe_2Ni_2$ [14], $CoFeNi_2V_{0.5}Nb_{0.75}$ [15] and $AlCrCuFeNi_2$ [16], etc. Among these eutectic HEAs, the $AlCoCrFeNi_{2.1}$ alloy received the most attention which solidifies into the softer FCC/$L1_2$ plus harder BCC/B2 eutectic structures, and the coupling effects of this eutectic structure endows the as-cast $AlCoCrFeNi_{2.1}$ eutectic HEA with a high strength and high ductility [17]. Further thermo-mechanical processing can achieve ultrafine-grained duplex and hierarchical microstructures which result in a further enhancement of the strength-ductility synergy [18].

Furthermore, it is worth noting that additive manufacturing (AM) of HEAs has recently attracted considerable attention worldwide [19]. In addition to the capability of near-net-shaping of complex geometry parts, the AM process is characterized by highly localized melting and solidification characteristic, which facilitates the formation of extremely non-equilibrium microstructures and may result in comparable or even better mechanical properties as compared with the counterparts processed by the conventional routes [20,21]. Several successful attempts to print HEAs have been made, including CrMnFeCoNi [22,23], CrFeCoNi [24], AlCoCrFeNi [25,26], $AlCoCrFeNiTi_{0.5}$ [27], compositionally graded HEAs [28,29] and laminated HEAs [30], etc.

Hydrogen embrittlement is a one-and-a-half-century-old problem

* Corresponding author.
E-mail address: di.wan@ntnu.no (D. Wan).

https://doi.org/10.1016/j.corsci.2021.110007
Received 27 May 2021; Received in revised form 17 September 2021; Accepted 2 December 2021
Available online 3 December 2021

that the hydrogen atoms in the environment may cause embrittling effects and catastrophic failure of metallic materials [31,32]. In the literature on the hydrogen embrittlement of traditional steels and alloys, several hydrogen embrittlement mechanisms have been proposed, including hydrogen-enhanced localized plasticity (HELP) [33–35], hydrogen-enhanced decohesion (HEDE) [36], hydrogen-enhanced super-abundant vacancies formation [37], adsorption-induced decohesion (AIDE) [38,39], and defect acting agent (DEFACTANT) concept [40], etc. However, due to the complexity of the problem, these mechanisms are not sufficient to universally explain this materials degradation phenomenon, and several attempts by combing two or more mechanisms have been proposed, such as the HELP-HEDE synergistic interplay [41] and HELP-mediated HEDE mechanism [42]. Generally, the most influencing factors on hydrogen embrittlement are environment, mechanical condition and material [43]. Therefore, high-strength materials are critical when serving in a H-containing environment, since they may experience a higher mechanical loading thus a higher susceptibility to hydrogen embrittlement due to their high strength. Among the high-strength materials, HEAs share a large portion owing to their rapid development. Recently, the mechanical behavior of the HEAs in the presence of hydrogen atoms has attracted increasing attention [44–47].

Despite the intensive research on hydrogen embrittlement in traditional alloys and a few recent studies on hydrogen embrittlement in FCC and BCC HEAs, the investigation on the effect of hydrogen on the mechanical behavior of eutectic HEAs is rather rare. In contrast to the hydrogen embrittlement of those single-phase FCC and BCC HEAs, the hydrogen embrittlement response of eutectic HEAs is more complex in view of distinct phases with different hydrogen diffusivity, different hydrogen solubility and thus different hydrogen response. When it comes to the eutectic HEA produced by AM techniques, the microstructural complexity generated during the unique processing routes makes the hydrogen embrittlement problem even more knotty.

Thus, in the current study, the $AlCoCrFeNi_{2.1}$ eutectic HEA is used as a platform to study the hydrogen embrittlement behavior in this field, which will provide understanding the hydrogen embrittlement effects in more complex HEAs rather than those single-phase FCC or BCC HEAs. Both conventional casting and AM processes are used to process the $AlCoCrFeNi_{2.1}$ eutectic HEA. The current study aims to investigate the hydrogen embrittlement behavior of $AlCoCrFeNi_{2.1}$ eutectic high-entropy alloy produced by AM. Pre-charged specimens as well as non-charged specimens are tested via small-scale in-situ tensile testing in a scanning electron microscope (SEM). Post-mortem characterizations including detailed fractography, electron backscatter diffraction (EBSD) and electron channeling contrast imaging (ECCI) are utilized to reveal the deformation and fracture performance. Thermal desorption spectroscopy (TDS) and finite element analysis (FEA) are adopted to understand the hydrogen uptake and distribution in the materials. Specimens from the as-cast material are also tested in the same sense to study the effect of microstructure in the hydrogen embrittlement performance of the investigated eutectic HEA. This study will deliver some basic inputs for further microstructural design of this eutectic HEA when severing in a H-containing environment.

2. Materials and experimental

Laser engineered net shaping (LENS™), a typical metal AM process, was used to process the $AlCoCrFeNi_{2.1}$ eutectic HEA. The LENS™ process produces metal parts by feeding powdered materials, with the aid of flowing argon gas, into a melt pool which is generated by a high-powered laser. The $AlCoCrFeNi_{2.1}$ prealloyed powder was prepared by plasma rotating electrode process (PREP), with the nominal composition of 16.39Al-16.39Co-16.39Cr-16.39Fe-34.43Ni (at%). A series of control experiments were performed at various laser powers, scan speeds, and hatch spacings. Based on the minimum defects, the following printing parameters were used to build the tensile specimen, i.e. a laser power of 400 W, scan speed of 5 mm/s, and a hatch spacing of 460 μm. The laser was scanned in a bi-directional and cross-hatched (i.e., a 90° rotation of the scan direction between successive layers) way, and such a scan strategy helps reduce the residual stress locked in the tensile specimen. Furthermore, the whole build process was performed in an enclosed chamber with oxygen content of below 20 ppm to minimize any potential oxidation.

It is worth noting that the eutectic structure in the currently studied alloy has been described in literature as FCC + B2 phases [48,49] or $L1_2$ + B2 phases [50]. In some literature the B2 phase was also described as a BCC phase [51]. The essential difference between these phases is that $L1_2$ and B2 phases are ordered phases with alternating atoms occupying different atomic sites, while FCC and BCC phases are disordered state with atoms equally occupying different atomic sites. The symmetry, however, remains almost the same between $L1_2$ and FCC or between B2 and BCC. Nevertheless, the ordering of the phases is not a focus of the current study, and differentiating the accurate symmetry does not contribute essentially to the hydrogen embrittlement behavior. Therefore, the phases in the current study are described as FCC/$L1_2$ and BCC/B2 hereafter to avoid controversy.

The specimens were cut by electron discharge machining (EDM) into a dog-bone shaped geometry with a gauge region of ~2.75 × 10 × 1 mm^3. The tensile specimens were prepared by grinding up to 4000 grit grinding paper followed by electropolishing in a H_2SO_4-methanol electrolyte. This electrolyte has been proven to provide good surface quality without residual strain from grinding in various materials such as ferritic silicon steel [52] and Ni and its alloys [53,54]. Due to the error in the machining process and the sample preparation, the dimension was measured individually before each tensile test started.

Hydrogen was pre-charged by electrochemical method using a glycerol-based electrolyte containing 600 g borax (sodium tetraborate decahydrate) dissolved into 1 L glycerol, plus 20 vol% distilled water and 0.002 M $Na_2S_2O_3$ as poison to enhance the conductivity and promote hydrogen absorption [55]. This electrolyte has the advantage of preserving the surface integrity during the charging due to its low solubility of oxygen. A platinum net was used as the counter electrode and Ag/AgCl was used as the reference electrode. Together with the specimen as the working electrode, a typical three-electrode electrochemical system was thus formed. The polarization curves of the studied materials are measured with the cell with a scan rate of 2 mV/s from − 3500–2500 mV (the potential value is reported with reference to Ag/AgCl hereafter) and can be found in the supplementary information. Galvanostatic condition was applied with the potentiostat for cathodic H-charging. The current density was controlled − 10 mA/cm^2, corresponding to a cathodic polarization potential of approx. − 2500 mV. The temperature of the electrolyte was controlled at 60 °C throughout the whole charging period of 50 h. After the electrochemical H-charging, the specimens were washed with distilled water and ethanol, then dried by circulating airflow. The dwell time between the end of H-charging and the start of the following testing was controlled to less than 5 min to minimize the hydrogen outgassing. It is worth noting that some surfaces changes can be induced solely by cathodic H-charging in some materials, e.g. surface cracks in Ni-based alloy 718 [54], surface steps in CoCrFeMnNi HEA [56] and martensitic transformation in Fe-30Mn-10Co-10Cr-0.5 C (at%) HEA [57]. While in the current study, the specimens did not show significant change in the surface integrity after the cathodic H-charging, and thus the behavior of materials observed in this work is categorized as the hydrogen-material interaction during deformation.

TDS was conducted on the H-charged materials to determine the hydrogen content and desorption behavior in the materials. The tests were conducted by a Bruker G4 PHONIX DH analyzer with a mass spectroscopy detector (ESD 100, InProcess Instruments, Germany) at a heating rate of 30 K/min from 25 °C to 650 °C. The dwell time between the end of H-charging and the start of the TDS tests was controlled to less than 5 min, similar to the case for tensile testing. Moreover, finite element method simulation was exploited to investigate hydrogen

diffusion process in both alloys (see supplementary information). The hydrogen contents were measured as 9.26 wppm and 12.03 wppm for the as-cast and AM materials, respectively, for the studied charging conditions.

The uniaxial tensile tests were performed on a tensile/compression module (Kammrath & Weiss GmbH, Germany) inside a Quanta 650 field emission gun (FEG) environmental scanning electron microscope (ESEM, Thermo Fisher Scientific Inc., USA). The tensile tests were conducted at room temperature with a constant displacement rate of 0.5 μm/s (corresponding to an initial nominal strain rate of $\sim 5 \times 10^{-5}$ s^{-1}). For in-situ imaging, an accelerating voltage of 20 kV was applied with an aperture of 30 μm and a spot size of 3.0. To characterize the microstructure, EBSD was conducted at an accelerating voltage of 20 kV, aperture of 100 μm and spot size of 4.0 at a working distance of about 17 mm. Additionally, ECCI was conducted at an accelerating voltage of 20–30 kV, aperture of 30 μm and spot size of 3.0 at a working distance of about 7 mm. The specimen was tilted to meet the two-beam diffraction condition in order to image crystallographic defects such as dislocations and stacking faults. More theoretical background regarding ECCI can be found in Ref. [58].

3. Results

3.1. Initial microstructure

Fig. 1 shows the microstructure of the as-received materials in as-cast state and AM state. The as-cast material has coarse solidification structure revealed as eutectic lamellae (width ~5 μm as shown in Fig. 1a and b) and large grain size (coarser than 500 μm[1]). Inside the FCC/$L1_2$ phase, residual dislocations (residual deformation) can be clearly observed that are straightly aligned along specific crystallographic planes (dashed lines in Fig. 1b). In contrast, the AM material shows much finer lamellae (width ~0.1 μm for B2/BCC and ~0.2 μm for FCC/$L1_2$) and smaller grain size (~10 μm), and the FCC/$L1_2$ phase shows a rather low dislocation density. Stacking faults can also be seen in the FCC/$L1_2$ phase of the AM specimen, but not in that of the as-cast specimen. The ultra-fine lamellae of the AM-ed specimens are attributed to the ultra-high cooling rate intrinsic to the LENS™ process, which was estimated to be the order of 10^3-10^4 K/s [59,60].

3.2. Mechanical performance

Fig. 2 shows the stress – strain curves from the in-situ uniaxial tensile tests. Clearly, the AM specimens showed higher strengths (both yield strength and ultimate tensile strength/ UTS) than the as-cast specimens. The yield strength increased from ~480 MPa (as-cast state) to ~820 MPa (AM state). No clear difference in yield strength can be seen between the H-free and H-charged specimens in both states. All the specimens showed strain hardening followed by sudden failure. No significant necking can be observed from the stress – strain curves, and therefore the ultimate tensile strength can be read from the stress level right before the failure, which is consistent with the cases of the same alloy system in literature [48]. For the as-cast state, the UTS decreased from 1007 MPa to 959 MPa (by ~5%) after H-charging; while for the AM state, it decreased from 1214 MPa to 1126 MPa (by ~7%) after H-charging. The elongation to failure with respect to the original gauge length (i.e. nominal strain to failure) was also changed significantly upon H-charging. For the as-cast state, the change was from 19.4% to 15.6%, and for the AM state it changed from 10.1% to 6.8%. The hydrogen embrittlement factor (*EF*) has been often used to describe the susceptibility of H-induced elongation/ strain loss [61] and is defined as Eq. 1, where $\varepsilon_{H-charged}$ and ε_{H-free} denote the strain to failure of the H-charged and H-free specimens, respectively. From the data, the as-cast material has an *EF*of 19.6% while that of the AM material is 32.7%, which means that the AM material is more susceptible to hydrogen embrittlement than the as-cast material in the current testing conditions. The properties are summarized in Table 1.

$$EF = \left(1 - \frac{\varepsilon_{H-charged}}{\varepsilon_{H-free}}\right) \times 100\% \quad (1)$$

3.3. Fractography

Fig. 3 shows the overview fractographs of the tested eutectic HEA specimens at relatively lower magnifications. In the as-cast state, the H-free specimen shows a similar transgranular-type ductile fracture in the overview (Fig. 3a), while the H-charged specimen shows some clear brittle features in the areas close to the specimen surface, as indicated by the white dashed lines in Fig. 3b. In the AM state, both the H-free and the H-charged specimens show brittle-like features in the overview (Fig. 3c & d), and more detailed views are presented at higher magnifications in Fig. 4 and Fig. 5. It is worth noting that the AM specimen has a globally brittle-like fracture surface regardless of H-charging, and therefore the H-induced brittle region and the corresponding influence depth cannot be easily defined from the fractography. Fig. 4 shows the fracture features of the H-free specimens. The as-cast specimen showed a mixed fracture type of both ductile dimples (Fig. 4a) and the so-called "herringbone" structure in the intra-dimple region (Fig. 4b). The "herringbone" structure is believed to be resulted from fracture along well-defined crystallographic planes (crack growth along <110> directions on {001} planes in BCC structures) and related to the microplastic deformation as well as local dislocation arrangement in the crack region [62]. The AM specimen shows primarily faceted brittle-like fracture patterns with ductile dimples in a comparable size with the brittle-like facets (Fig. 4c). When looking into the facets, some "tree-ring" structures can be seen obviously (Fig. 4d). After hydrogenation, substantial difference can be found in the fractographic features. In the as-cast specimen, some quasi-cleavage features can be found close to the surface of the specimen, as shown in Fig. 5a. Further away from the surface, the features change gradually from quasi-cleavage to large dimples, and the size of dimples becomes smaller when further into the center of the specimen. When observed at a higher magnification, the large dimples in the H-charged as-cast specimen show a mixed feature of dimple boundaries formed by shearing and intragranular secondary cracks in the intra-dimple regions (Fig. 5b), which are missing in the H-free specimens (Fig. 4a and b). Some slip lines can also be observed in the intra-dimple regions accompanying the secondary cracks, though not very drastically. The AM specimen shows pure faceted fracture feature, and no significant transition can be extracted when observing along the thickness direction (Fig. 5c). The whole fracture surface, however, seems to be more flat than that of the H-free specimen. At a higher magnification, straight slip lines can be observed on the flat faceted fracture surface (Fig. 5d), in contrast to the curved slip lines in the H-free case (Fig. 4d). It needs to mention that the phases in the fractography was determined based on the morphology taken from top-surface investigations, the phase fraction, and the different fracture behavior (cf. characterization results in the following sections).

3.4. Surface cracks

From the in-situ videos of the tensile testing (see supplementary files), the major divergence in the H-charged specimens is the appearance of a large amount of surface cracks after the material yields. Fig. 6 shows a collection of the surface cracks in H-charged specimens in both as-cast state and AM state. In the as-cast specimen, a clear phenomenon is that the FCC/$L1_2$ phase has been more drastically deformed with

[1] Due to the limited imaging size and the purpose of showing the eutectic lamellar structure, Fig. 1a was taken inside a single grain and thus the grain size cannot be estimated from this figure. The coarse grain size has been determined by large-area EBSD scans, which are not shown in the paper.

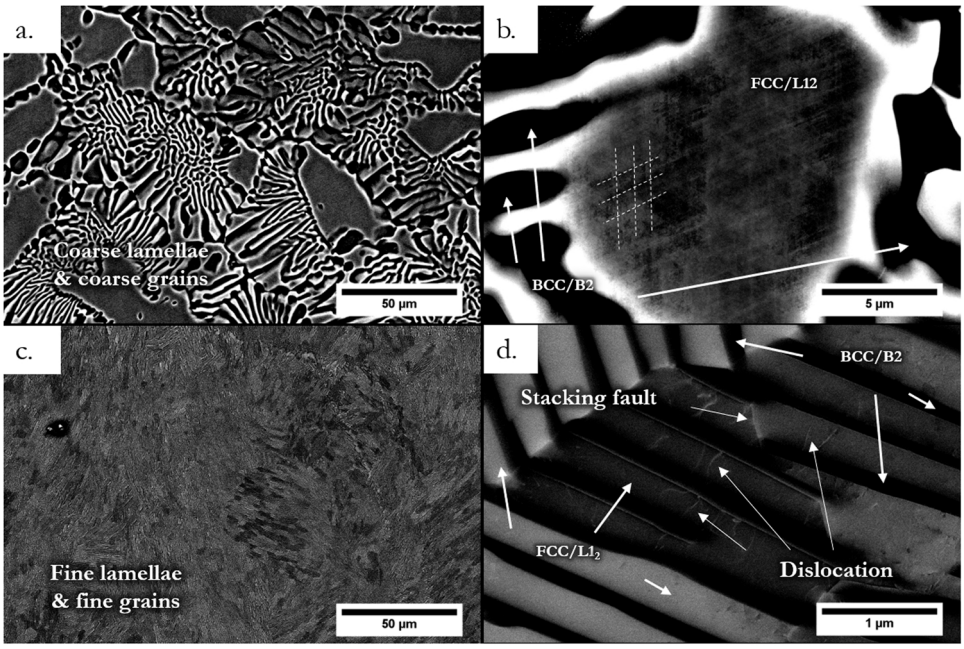

Fig. 1. ECC images on the initial microstructure of the eutectic HEA specimens before tensile test: a&b. as-cast state; c&d. additive manufactured.

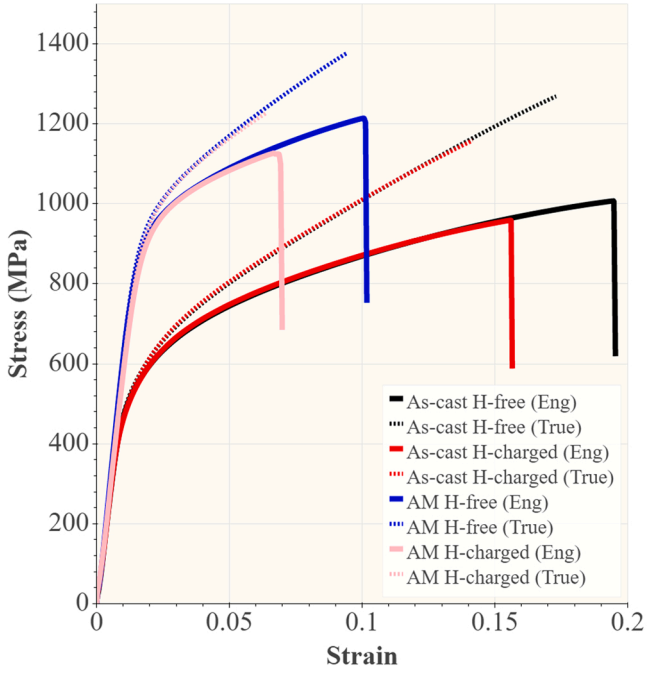

Fig. 2. Stress vs. strain curves from the uniaxial tensile tests.

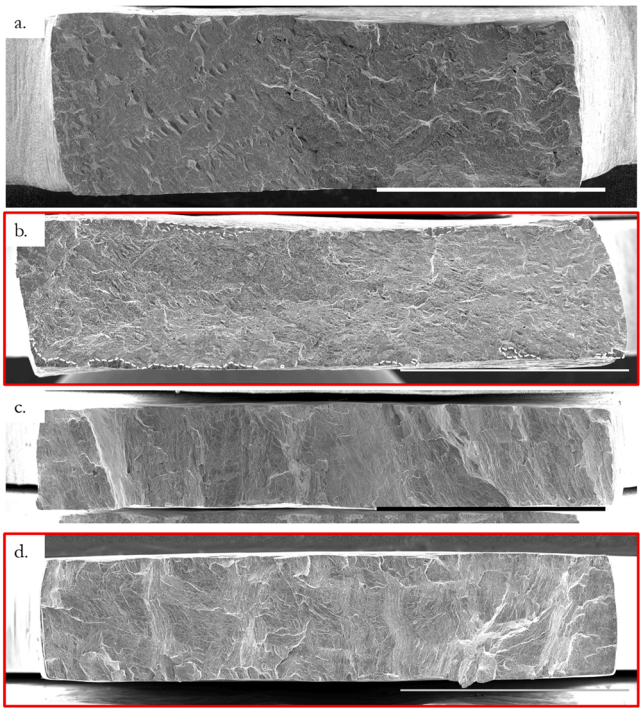

Fig. 3. Overview fractographs of the tested specimens: a. as-cast, H-free; b. as-cast, H-charged; c. AM, H-free; d. AM, H-charged. The scale bars in the figures indicate 1 mm.

Table 1
Mechanical properties from the in-situ tensile testing.

Specimen	As-cast		AM	
Testing condition	H-free	H-charged	H-free	H-charged
Yield strength/ MPa	480	480 (-)	820	820 (-)
Ultimate tensile strength/ MPa	1007	959 (↓5%)	1214	1126 (↓7%)
Strain to failure/ %	19.4	15.6	10.1	6.8
Embrittlement factor	19.6%		32.7%	

evident slip traces on the surface, and the surface cracks seem to be initiated in the BCC/B2 phase and propagated along the phase boundaries (PBs) or slip traces (Fig. 6a and b). In the AM specimen, in the same way, most of the surface cracks can be found in the BCC/B2 phase, and the propagation follows the PBs between the FCC/L1$_2$-BCC/B2 phases (Fig. 6c and d).

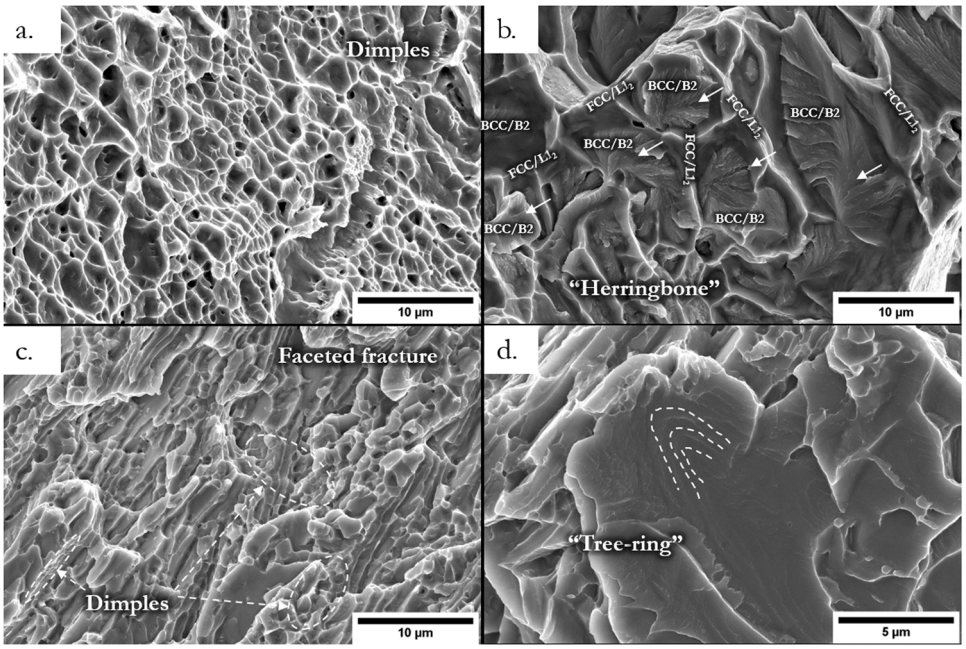

Fig. 4. Detailed fractographs of the tested specimens (H-free): a&b. as-cast; c&d. AM. The white arrows in b indicate the "herringbone" structure. The highlighted regions by dashed lines and arrows in c indicate ductile dimples. The marks in d indicate the "tree-ring" structure.

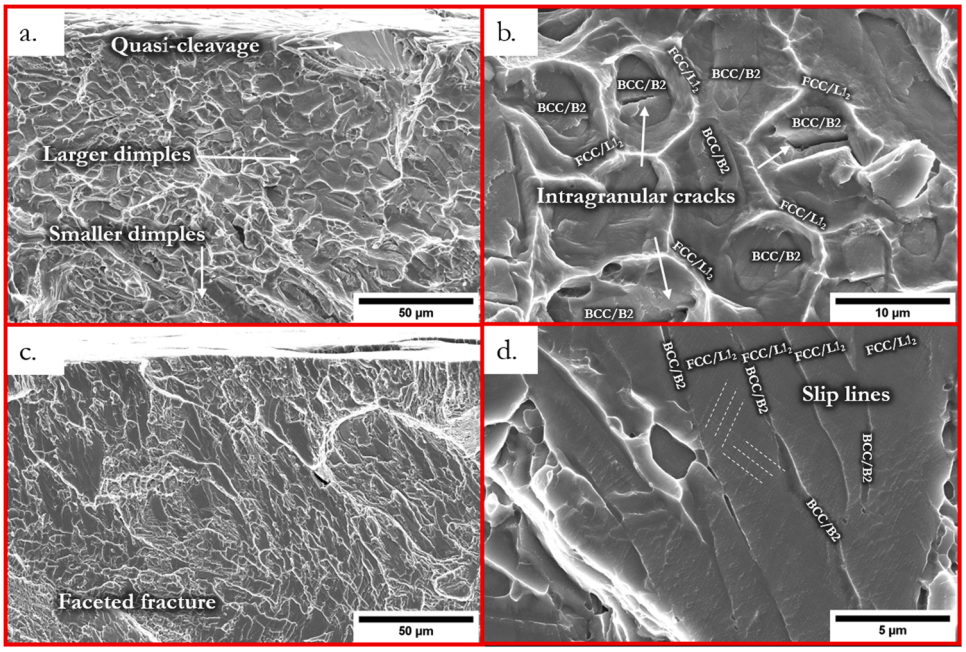

Fig. 5. Detailed fractographs of the tested specimens (H-charged): a&b. as-cast; c&d. AM.

3.5. Microstructure evolution

Fig. 7 shows the deformation structure of the AM specimen after tensile test. The dislocation density has increased in both the H-free and the H-charged specimens in comparison with the initial microstructure in Fig. 1d. Stacking faults also increased the amount, and nano-twin started to appear in both specimens. Newly formed dislocation loops can be captured in the H-free specimen (Fig. 7b). A unique feature observed in the H-charged specimen is the surface crack, as indicated by the dotted lines in Fig. 7c. A deformation-concentrated zone can be documented close to the surface crack.

3.6. Hydrogen diffusion

The hydrogen content and desorption behavior of the investigated eutectic HEA were studied via TDS measurements. The measured hydrogen contents are 9.26 wppm and 12.03 wppm for the as-cast and AM materials, respectively, after 50 h H-charging. To estimate the hydrogen distribution in the bulk material, a "thick-plate model" (i.e. semi-infinite assumption) was adopted for showing the case that external hydrogen slowly diffuses into a thick wall or pipe section [63]. The hydrogen concentration can be described by the following mathematical expressions:

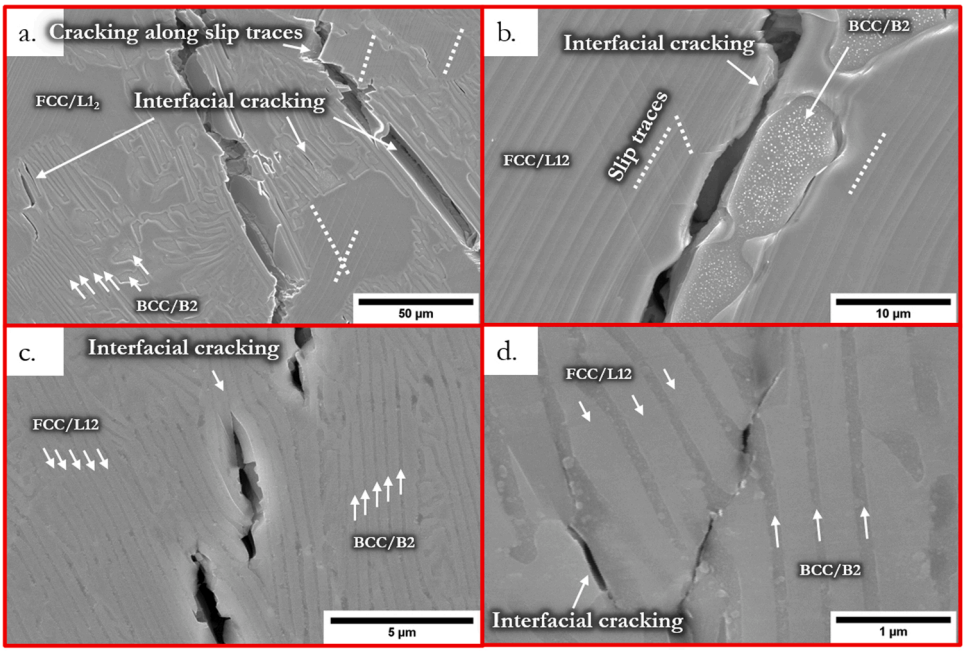

Fig. 6. Surface cracks on the top surface of the H-charged tensile specimens after in-situ tensile testing. a&b. as-cast state; c&d. AM state. The dotted lines show the slip traces. The global tensile direction is horizontal.

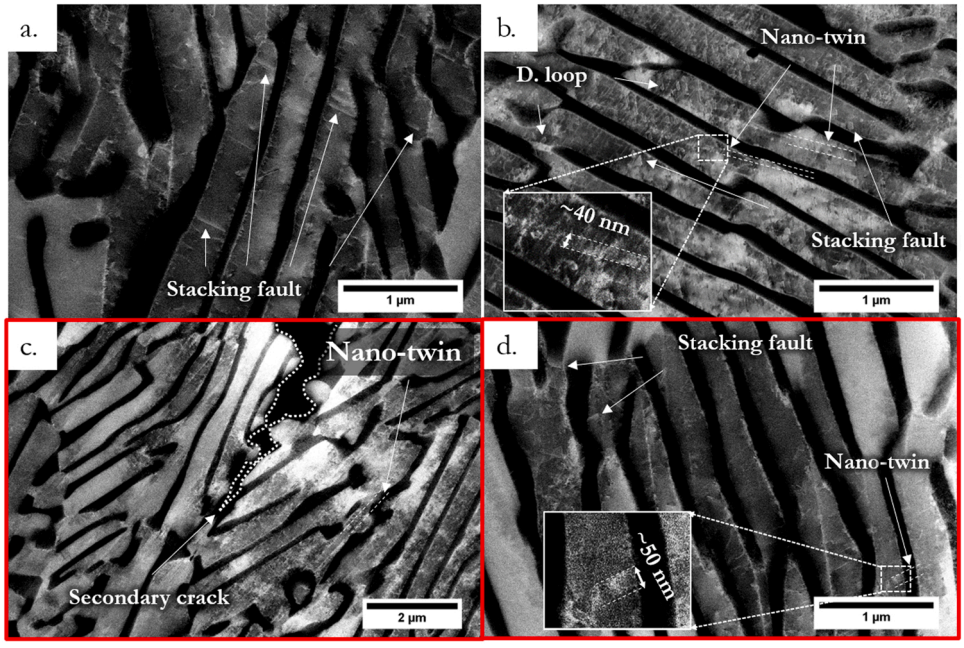

Fig. 7. ECC images on the deformation microstructure of the AM eutectic HEA specimens after tensile test: a&b. H-free; c&d. H-charged. "D. loop" stands for dislocation loop. The global tensile direction is horizontal.

$$\frac{C(x,t)-C_0}{C_i-C_0}=1-\mathrm{erf}\left(\frac{x}{\sqrt{4Dt}}\right) \tag{2}$$

where

$$\mathrm{erf}(u)=\frac{2}{\sqrt{\pi}}\int_0^u \exp\left(-u^2\right)\mathrm{d}u \quad \text{and} \quad u=\frac{x}{\sqrt{4Dt}} \tag{3}$$

In Eq. 2 and Eq. 3, $x$is the distance to the surface of the specimen; t is the time of the H-charging; and thus $C(x,t)$ denotes the hydrogen concentration at the distance x inside the material after t time of charging. C_0 is the initial bulk hydrogen concentration, which is assumed to be 0 in the current study. C_i is the constant surface hydrogen concentration as assumed in the thick-plate model. $D$is the diffusivity of hydrogen in the material. A recent study by Turk et al. [64] has shown that when multi-phases are presented in an alloy, the effective hydrogen diffusivity becomes heavily dependent on the morphology of the phases and the conditions of the interfaces, and the assumption of negligible concentration gradient in the fast-diffusion phase (i.e. ferrite in the dual-phase steel in Ref. [64] or the BCC/B2 phase in the current study) is a poor approach. Unfortunately, to the best of the authors' knowledge, due to the lack of studies and the complexity of the microstructure, the accurate hydrogen diffusivity is not available in literature yet. However, another

recent study on a duplex stainless steel [65] shows that the apparent hydrogen diffusivity in the equi-volumeric ferrite-austenite dual-phase matrix is in the order of 10^{-15} m^2/s by using finite element method. Considering the volume fractions of the FCC/$L1_2$ (~65%) and BCC/B2 phases (~35%) [50,66] in the studied alloy, an effective diffusivity is assumed to be in the order of 10^{-15} m^2/s (after considering the charging temperature at 60 °C). Therefore, the hydrogen concentration profile can be calculated. Based on this calculation, most of the hydrogen is accumulated in the first ~50 μm immediately below the surface of the specimen. (see supplementary information).

3.7. Post-deformation EBSD characterization of the AM specimens

EBSD was performed on the deformed AM specimens for deeper analysis of the deformation behavior, cracking behavior, and boundary characteristics. Fig. 8 presents the EBSD maps of the failed AM specimens in both H-free and H-charged cases. In the H-free case, no surface cracks can be found, while surface cracks can be clearly seen along PBs or GBs in the H-charged AM specimen. Fig. 9 shows the IPF-Z map, phase map, and selected pole figures of the AM specimen for orientation relationship determination between the FCC/$L1_2$ and the BCC/B2 phases. From the pole figures, the {110} and {111} poles of the FCC/$L1_2$ phase are overlapping with the {111} and {110} poles of the neighboring BCC/B2 phase, corresponding to the Kudjumov-Sachs (K-S)-type orientation relationship. Fig. 10 shows two typical areas showing surface cracks of the tensile-deformed H-charged AM specimen in terms of IPF-Z maps. The crystallographic properties of these surface cracks are further analyzed and discussed in Section 4.3.

4. Discussion

4.1. Deformation and fracture behavior of the eutectic HEA

Apparently, the studied eutectic HEA shows valuable mechanical properties both in the as-cast (yielding at ~480 MPa, UTS at ~1007 MPa and failure at ~25.9% elongation) and AM states (yielding at ~820 MPa, UTS at ~1214 MPa and failure at ~13.5% elongation) when hydrogen is absent. Several reasons can be attributed to this excellent properties combination. The eutectic HEA has a heterogeneous microstructure consisting of a relatively soft FCC/$L1_2$ phase and a relatively hard BCC/B2 phase. It is reasonable to speculate that the soft FCC/$L1_2$ phase yields earlier upon loading, than the BCC/B2 phase. The mechanical incompatibility between the two phases can result in a strain gradient and thus needs extra geometrically necessary dislocations (GNDs) to accommodate the deformation at the boundaries. The GND pile-up at the PBs will consequently create a long-range back-stress, and thus causing the so-called back-stress strengthening [49,67]. This strengthening mechanism can also prevent strain localization (necking) and thus increasing the ductility. Comparing the microstructures of the studied materials in both as-cast and AM states, that of the AM state has much finer lamellae and fine grains, while the as-cast state has coarse lamellae and coarse grains (see Fig. 1). Therefore, apart from the conventional strengthening mechanism of grain refinement, it is reasonable to think that the back-stress strengthening contributes to the higher strength and decent ductility of the AM eutectic HEA. Furthermore, the semi-coherent PBs between the phases [68] and solid solution and precipitates hardening [68] in the respective phase constituents have also been uncovered in literature. In the FCC/$L1_2$ phase of the AM specimen, the dominant deformation mechanisms are (planar) dislocation glide and stacking faults as can be seen in Fig. 7a and b, and a

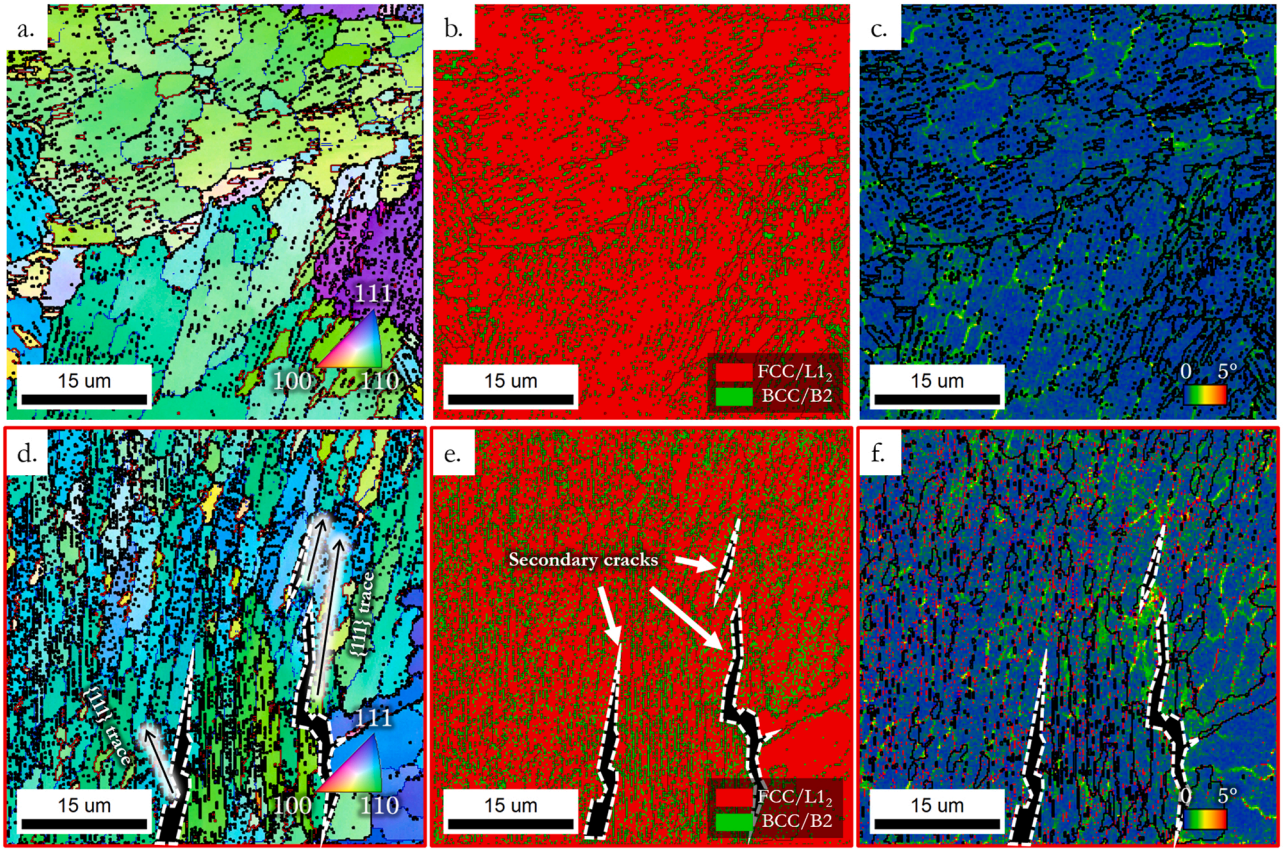

Fig. 8. EBSD maps of the tensile-deformed AM specimens. a-c. from the H-free specimen; d-f. from the H-charged specimen. a&d. IPF-Z map; b&e. phase map; c&f. KAM map. The global tensile direction is horizontal.

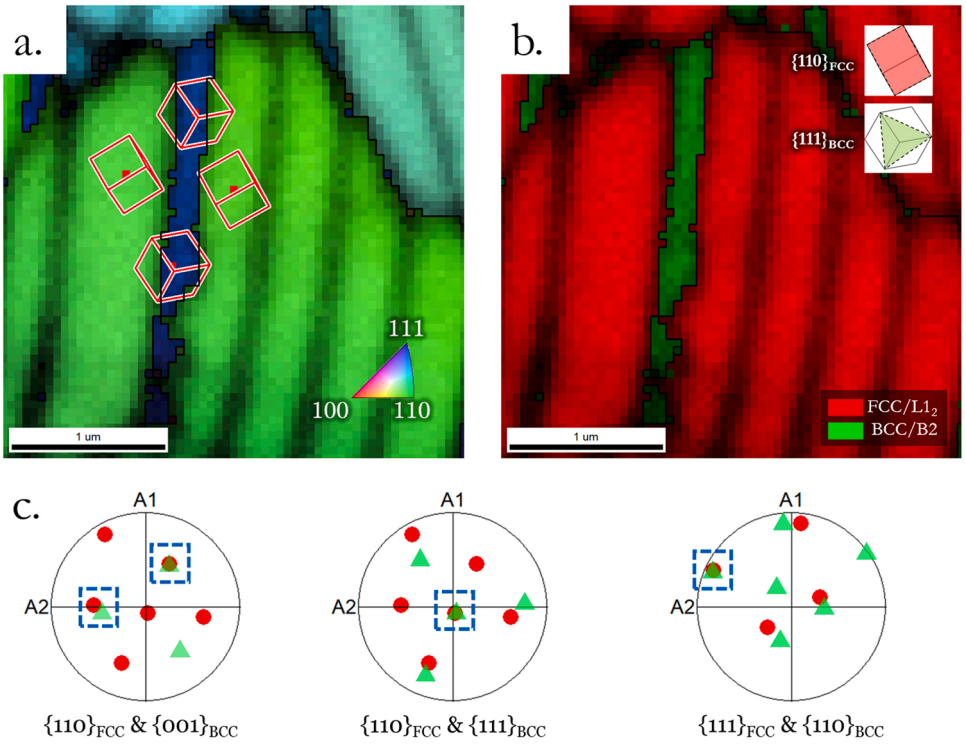

Fig. 9. Orientation relationship determination in the AM specimen: a. IPF-Z map; b. phase map; c. pole figures showing the poles from the highlighted points in a.

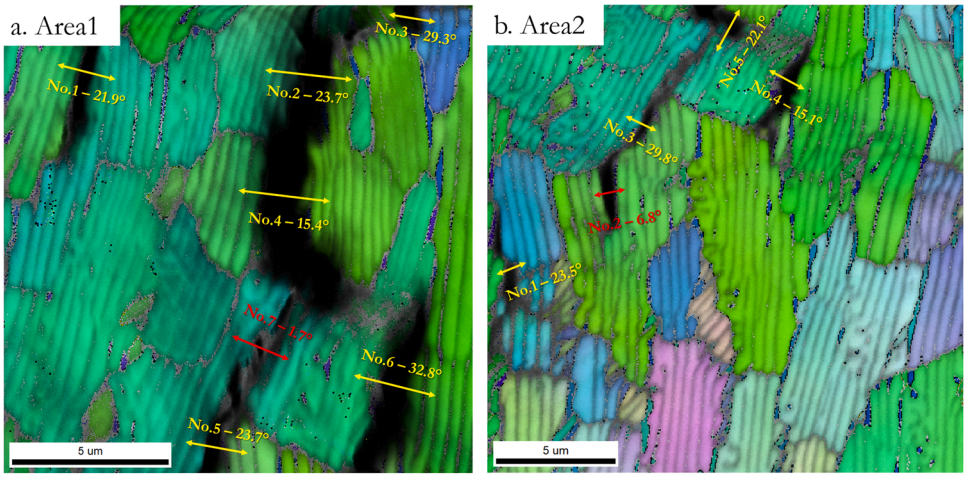

Fig. 10. EBSD IPF-Z maps of the tensile-deformed H-charged AM specimens in two areas with surface cracks. The corresponding misorientation has been marked across the cracks.

relatively higher dislocation density can be seen close to the PBs, which is in agreement with the results from literature [48,68] and in line with the back-stress strengthening mechanism mentioned above. It is also clear in the supplementary video (EHEA_as-cast_H-free.mp4) that the FCC/$L1_2$ phase showed the slip lines have a single dominant direction, and the second slip line direction appeared only shortly before the final fracture, confirming the planar slip characteristics of the FCC/$L1_2$ phase in this alloy. In the BCC/B2 phase of the AM specimen, only dislocations are found, with occurrence of their being pinned by nano-precipitates [68].

Supplementary material related to this article can be found online at doi:10.1016/j.corsci.2021.110007.

Supplementary material related to this article can be found online at doi:10.1016/j.corsci.2021.110007.

Supplementary material related to this article can be found online at doi:10.1016/j.corsci.2021.110007.

Based on the stress-strain curves in Fig. 2, the current alloy does not have a good resistance to crack growth as soon as the UTS has been exceeded upon loading. All the tested cases showed sudden failures, as can also be indicated in the supplementary videos. From the fractographs, one can see that for the H-free case, the FCC/$L1_2$ phase mainly shows ductile fracture behavior such as dimples or tearing ridges (Fig. 4), but the BCC/B2 phase fails with a brittle-like manner in the form of "herringbone" and faceted fracture features. From Fig. 4b and d, the fracture in the BCC/B2 phase seems to initiate from one interface connecting the FCC/$L1_2$ phase and then propagated through the whole BCC/B2 phase, forming either river patterns (or "herringbones") or the "tree-ring" patterns. This implies that the stress accumulated at the PBs

could have initiated cracking in the BCC/B2 phase as it is less ductile than the FCC/$L1_2$ phase. When the BCC/B2 phase fails, the stress will be taken over by the softer FCC/$L1_2$ phase. This high stress level rapidly makes local necking happening in the FCC/$L1_2$ phase, thus leading to a sudden failure of the whole specimen. An interesting fact is that the FCC/$L1_2$ phase sometimes forms only tearing ridges but not dimples, which happens in the as-cast specimen with coarse grain and phase sizes (Fig. 4b). This could possibly be explained as below. After the failure of the brittle BCC/B2 phase, the stress is first transferred to the PB of the FCC/$L1_2$ grain, and the dislocation slip starts from the boundary and propagates inwards. Due to the coarse size of the phases, there is a stress gradient between the edge and the center of the FCC/$L1_2$-phased grain, and since this phase is deformed dominantly by planar slip, the deformation prefers to propagate in a single direction or limited directions. This applies also to the neighboring PBs, and therefore, the FCC/$L1_2$ grains shear from their edges into the center and form the single tearing ridge shown in Fig. 4b. This tear ridge – fishbone alternating fracture mode has also been observed in the same alloy with lamellar structure [68] and an Al-Si alloy with similar eutectic structure [69].

On the other hand, the phase morphology can be an influencing factor of the local stress state and thus influencing the deformation and damage mechanisms. It has recently been discovered that the lamellar orientation in the studied alloy has a strong effect on the deformation and fracture behavior due to the dislocation – interface interactions

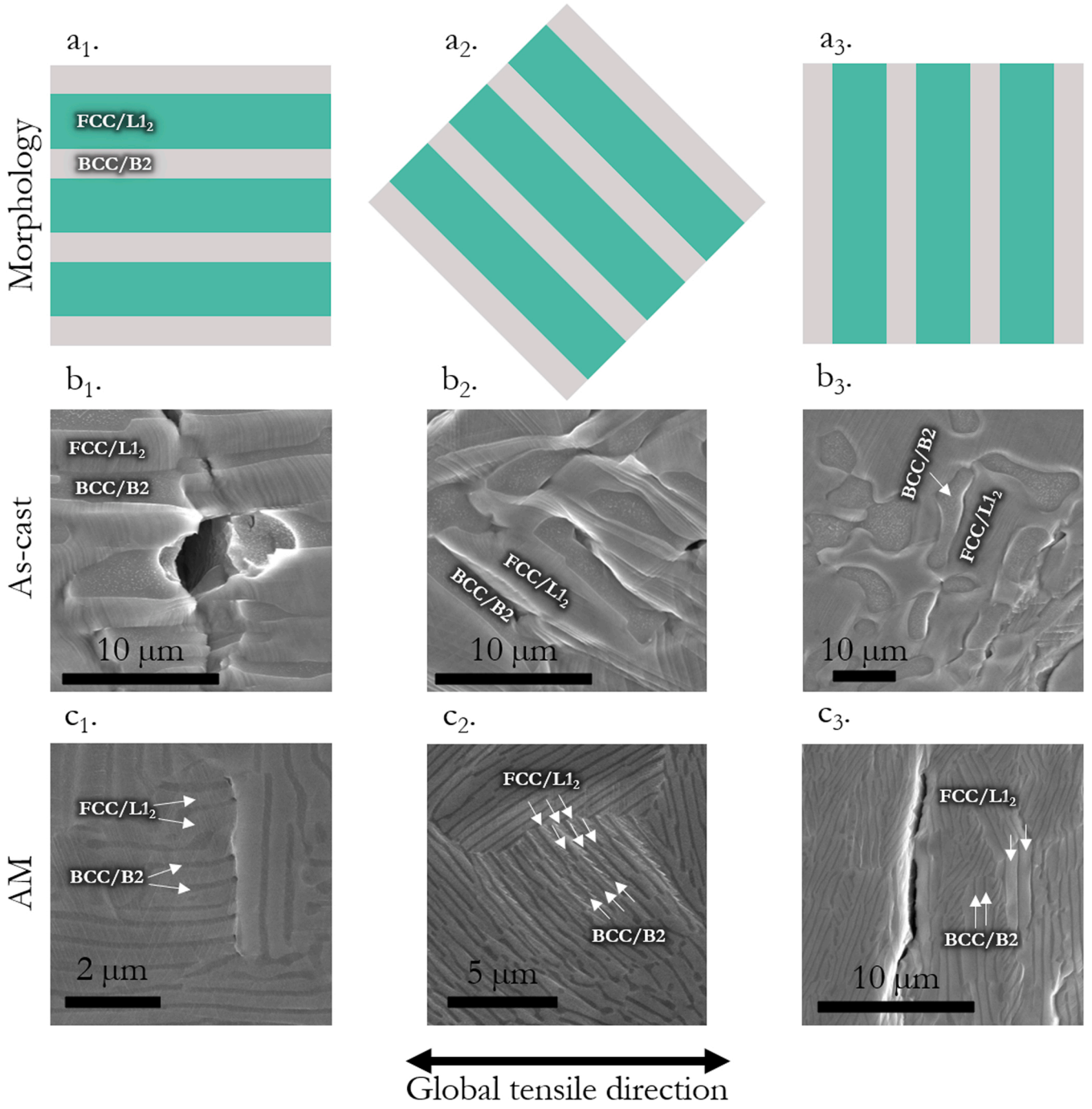

Fig. 11. Representative cases showing the phase morphology dependence of the deformation and crack initiation. a_1-a_3: representative phase morphology; b_1-b_3: exemplary SEM images of the as-cast specimen; c_1-c_3: exemplary SEM images of the AM specimen. The global tensile direction is horizontal.

[70]. Fig. 11 summarizes three typical morphologies with the deformation and cracking examples in the studied alloy both in as-cast and AM states. When the phases are roughly parallel to the tensile direction, both the as-cast and the AM specimens show crack initiation in the BCC/B2 phase and propagation perpendicular to the loading direction (Fig. 11 b_1 and c_1). This is in line with the fact that the BCC/B2 phase has a lower ductility in comparison with the FCC/$L1_2$ phase. When the phases are roughly along 45° to the tensile direction, the crack initiates from the PBs and propagates either along the PB or along the shearing direction in the BCC/B2 phase of the as-cast specimen (Fig. 11 b_2). While in the AM state, a clear deformation accumulation can be seen in the FCC/$L1_2$ phase towards the BCC/B2 phase, and the deformation is stopped by the grain boundary (GB), but no significant crack initiation is observed (Fig. 11 c_2). When the phases are close to the perpendicular direction to the tensile direction, both the as-cast and the AM specimens show crack propagation along PBs (Figure 11b_3 and c_3).

4.2. Hydrogen diffusion in the eutectic HEA

Due to the complex microstructure of the investigated eutectic HEA, a simple number of the hydrogen content is not enough to describe the scenario in the material, and therefore, the combination of TDS measurement and FEA diffusion analysis (see the supplementary information) was adopted in the current work to interpret the hydrogen diffusion behavior. From the results, the AM material contained a larger amount of hydrogen (12.03 wppm) than the as-cast material (9.26 wppm) by about 30%. According to a study by scanning Kelvin probe force microscopy (SKPFM), hydrogen prefers to be trapped at PBs between γ-austenite and strain-induced α'-martensite in a deformed 316 L austenitic steel [71]. Since the phase structure in the current eutectic HEA is similar as a combination of γ-austenite and α-ferrite or α'-martensite, it is reasonable to consider the PBs in the eutectic HEA are favorable hydrogen trapping sites. Therefore, the larger amount of PBs in the AM state naturally explained the stronger hydrogen trapping effect and the higher amount of hydrogen detected by TDS.

Owing to the sharp difference between the hydrogen behavior in the FCC/$L1_2$ phase and in the BCC/B2 phase, the final hydrogen distribution in the material is extremely inhomogeneous. The simulation results provide some evidence for the inhomogeneous hydrogen distribution and trapping. Locally, the FCC/$L1_2$ phase was not saturated while the BCC/B2 phase can be supersaturated. Therefore, the PBs can be the location with intense hydrogen concentration gradient and ideal for hydrogen trapping [72]. The different diffusion length between the as-cast microstructure and the AM microstructure should be resulted from the different amount of PBs on the diffusion path as they can act as hydrogen trapping sites and obstacles for hydrogen diffusion [73]. In the as-cast microstructure, the PBs are more or less homogeneously distributed without a significantly preferred orientation profile and thus the diffusion paths are similar when changing the diffusion directions, but the AM microstructure has distinct lamellar structure that has less PBs along the lamellae and more PBs across the lamellae. When diffusing along the lamellar direction, the hydrogen encounters weaker trapping by the PBs and thus diffuses further, and vice versa. This explains the different scenarios of the austenitic phases in the FEA analysis (see supplementary information). For the ferritic phase, the difference is not as distinguishable as the austenitic phase, probably because of the high hydrogen diffusivity and the low hydrogen solubility. Additionally, the difference in the amount of PBs gives a hint on the different embrittlement factor between the as-cast and the AM specimens: more PBs trap more hydrogen and thus making the specimen becomes more prone to H-induced effects.

Apart from the hydrogen trapping at boundaries, a higher strength level can also contribute to the hydrogen embrittlement susceptibility. It has been in-situ confirmed that hydrogen prefers to migrate to the region under higher stress level via the Gorsky effect [74]. In the current study, the AM specimen has a larger amount of boundaries as well as a higher strength level than the as-cast specimen. Therefore, the hydrogen can more easily follow the stress field in the stronger AM specimen and cause a more severe hydrogen embrittlement susceptibility.

4.3. Hydrogen influence on the deformation of the AM eutectic HEA

The studied alloy in both as-cast and AM states showed occurrence of secondary surface cracks during tensile deformation, especially in the later stage of the deformation (see the supplementary videos). Similar phenomena have been observed by the current authors in a Ni-based superalloy [54] and a twinning-induced plasticity (TWIP) steel [55]. A closer look into the surface cracks shows that they start predominantly along the boundaries between the FCC/$L1_2$ and the BCC/B2 phases (Fig. 6). A detailed EBSD scan on the deformed AM specimen in Fig. 8 also confirms the findings: without H-charging, no surface cracks can be found; after H-charging, surface cracks can be found along PBs or GBs. It is also found that the primary direction of the surface cracks are approximately along the {111} traces (i.e. the slip traces of the FCC/$L1_2$ crystals) of the neighboring FCC/$L1_2$ phase when the cracks are propagating in a transgranular manner. When the cracks are meeting PBs, the propagation direction can be deviated. This seems to be in-line with both the HELP and the HEDE mechanisms. In the FCC/$L1_2$ phase, hydrogen localizes the deformation to limited slip systems such that local deformation becomes severe and local necking + failure happens, which leads to cracking along slip traces (the {111} traces observed in Fig. 8d). On the other hand, hydrogen also weakens the bonding energy of the boundaries such that when cracks are approaching, the boundaries become more easily to be opened by the stress field associated with the cracks. One can see both the HELP and the HEDE mechanisms are activated in a typical manner in the current alloy. In the recent years, the synergistic effect of different hydrogen embrittlement mechanisms has been proposed to play an important role in the failure procedure of materials served in a H-containing environment. The typical ones are HELP + HEDE synergy and HELP-mediated HEDE models [75–77].

A complexity remains here is the hydrogen embrittlement susceptibility of the different types of boundaries. Based on the SEM observation in Fig. 6, the surface cracks seem to be initiated from the BCC/B2 phase or from the decohesion of the PBs. One reason could be that the hydrogen trapping at PBs results from the accumulation of hydrogen between two phases with extremely different hydrogen diffusivities and solubilities (see the simulated scenarios in the supplementary document). On the one hand, the less ductile BCC/B2 phase can easily be embrittled and initiate cracks from the phase interior, which can be correlated with the quasi-cleavage fracture in Fig. 5a and the intragranular cracks in Fig. 5b; on the other hand, the PBs can also be embrittled based on the HEDE mechanism, which can explain the interfacial cracking generally observed on the surfaces (Fig. 6). However, the GBs can also play an important role in the hydrogen embrittlement behavior. It has been reported that hydrogen can be trapped at GBs results from the hindering effect of the boundaries and the mismatch between the diffusivities of different crystallographic orientations [78]. It can be taken into consideration that during deformation, dislocations cannot easily pass the GBs due to the lattice mismatch, and thus piling up at the boundaries. Generally dislocations are recognized as hydrogen trapping sites and can induce hydrogen embrittlement in the material [61]. The H-trapped dislocation pile-ups at the GBs can be considered as responsible for the GB-type cracking.

It has been reported that the investigated eutectic HEA can have a Kudjumov-Sachs (K-S)-type orientation relationship (OR) between the FCC/$L1_2$ and the BCC/B2 phases based on the diffraction analysis in transmission electron microscope [79]. Fig. 9 shows the OR determination by EBSD in the AM eutectic HEA. The OR shows roughly $< 110 >_{FCC}//< 111 >_{BCC}$ and $\{111\}_{FCC}//\{110\}_{BCC}$, which is in agreement with the K-S-type OR. As is known, $< 110 >$ is the dislocation slip direction in FCC structures and $< 111 >$ in BCC structures. The K-S OR can help dislocations passing through the PB or emitting from the PB in

the dual-phase microstructures such as the investigated eutectic HEA [70]. Furthermore, a $< 110 >_{FCC}//< 100 >_{BCC}$-type OR can also be noticed as shown in Fig. 9c. It can be speculated that the dislocations slip along the $< 110 >$ directions in the FCC/$L1_2$ phase, and are stopped by the PB with the $< 100 >$ direction continuing in the BCC/B2 phase. First of all, the dislocation – PB interaction can create a locally high stress field when the dislocations cannot easily pass through the boundary, and cause local deformation in the neighboring phase/ grain. This can probably be the cause of the "herring-bone" fracture features in Fig. 4b where cleavage-type can be noted in the BCC/B2 phase. Secondly, the locally accumulated hydrogen at the PB can cause a weakening of the PB cohesion energy due to the HEDE mechanism. Finally, the {100} planes cleave more easily from the combination of high stress by dislocations and weak cohesion by hydrogen and leave the brittle fracture features in the BCC/B2 phase in Fig. 5. In Addition, the straight slip lines observed on the fracture surface the FCC/$L1_2$ phase also give a hint towards the assumption of dislocation-PB interaction.

To find the crystallographic properties of the H-induced surface cracks, EBSD has been further performed in selected areas with the cracks. Fig. 10 shows two exemplary areas with the misorientation information summarized in Table 2. Among the 12 cracks analyzed, 10 of them (~83.3%) can be recognized as random high-angle grain boundaries (HAGBs, misorientation>15°) without noticeable coincident site lattice (CSL) relationships, and two of them are low-angle grain boundaries (LAGBs, misorientation<15°). Furthermore, the cracked LAGB No.7 in Area1 (Fig. 10a) seems to be a linkage between the cracks from No.4 and No.5, but not directly a H-induced cracking. Moreover, the boundary No.2 in Area2 (Fig. 10b) is seems to result from the PB decohesion that was influenced by the crack propagation from No.3. Most of the surface cracks (7 out of 12, ~58.3%) are having a misorientation angle of about 20–30° (Table 2). Apart from No.2 in Area2, there is hardly a perceptible trend of PB cracking in the investigated regions. As a short conclusion, the normal HAGBs are more susceptible to hydrogen embrittlement than the PBs in the AM eutectic HEA, probably due to the dislocation interaction at the boundaries mentioned above.

Without hydrogen charging, the AM specimen was mainly deformed by dislocation slip, stacking fault and nano-twin formation. When hydrogen has been charged into the material, the deformation mechanisms did not change significantly. One observable difference is the formation of dislocation loops. In the H-free case, some dislocation loops are found in the FCC/$L1_2$ grains, but they are not clearly found in the H-charged case. A possible reason is that hydrogen has an effect of lowering the stacking fault energy of the material [80]. The perfect dislocation loops can easily form partial dislocations, and thus full dislocation loops are absent in the H-charged specimen. The dislocations in the FCC/$L1_2$ phase of this material mainly slip in a planar manner. The planar slip nature of the dislocation patterns observed in Fig. 7 (i.e. Taylor lattice [81]) also provides proofs on lowing the stacking fault energy by hydrogen. Furthermore, the marks on the fracture surfaces of the FCC/$L1_2$ phase in Fig. 4d and Fig. 5d proves that the dislocations can slip in a curved way in the H-free case and form the "tree-ring" structures. After H-charging, the dislocations slip dominantly along specific directions and form the straight marks on the fracture surface. This dislocation behavior can be explained by the HELP mechanism that the slip will be limited to particular directions (e.g. Ref. [35]).

Recent studies show that in multi-phase materials, both the phase morphology [82] and the chemical variation [83] can significantly influence the mechanical performance of the material. The current study provides a detailed analysis on the hydrogen embrittlement behavior of AM eutectic HEA, where the boundary types are also found to be contributing to the cracking susceptibility. It can be suggested that when designing practical component for real-life applications in a hydrogen-containing environment using AM technique, such behavior should be considered for the in-service parts. Combining with AM technique and subsequent thermo-mechanical processing, it is highly promising to develop components with better resistance against environmental degradation.

Table 2
Misorientation across the surface cracks in Fig. 10.

Area	Crack No.	Misorientation (°)	Boundary Type
Area 1	1	21.9	HAGB
	2	23.7	HAGB
	3	29.3	HAGB
	4	15.4	HAGB
	5	23.7	HAGB
	6	32.8	HAGB
	7	1.7	LAGB
Area 2	1	23.5	HAGB
	2	6.8	LAGB
	3	29.8	HAGB
	4	15.1	HAGB
	5	22.1	HAGB

5. Conclusions

In the current study, the hydrogen embrittlement behavior of one kind of $AlCoCrFeNi_{2.1}$ eutectic HEA manufactured by AM have been studied via small-scale in-situ tensile testing with and without cathodic H-charging. As-cast specimens were also tested as a reference. The deformation and fracture behavior has been investigated via SEM-based techniques including fractography, EBSD and ECCI. The hydrogen trapping and diffusion behavior has been studied by TDS and FEA. Some conclusions are drawn as follows:

1. The AM eutectic HEA has a higher tensile strength but a lower ductility than the as-cast material. The higher strength of the AM eutectic HEA can be explained by the back-stress strengthening and grain refinement. The failure of the specimens can be explained by the PB decohesion and the consequential failure of the BCC/B2 phase for both AM and as-cast states.
2. The H-charged AM eutectic HEA shows a decrease in the strain to failure from 10.1% to 6.8% with an embrittlement factor of about 32.7%, whereas the as-cast specimen shows that from 19.4% to 15.6% with an embrittlement factor of about 19.6%. Both specimens show a decrease in the UTS (from 1214 MPa to 1126 MPa for the AM specimen and from 1007 MPa to 959 MPa for the as-cast specimen), but not significantly in the YS (820 MPa for the AM specimen and 480 MPa for the as-cast specimen).
3. The H-charged specimens show surface cracks when subjected to tensile deformation, which is absent in the H-free specimens. This can be the reason for the decreasing UTS.
4. After the same charging sequence, a higher amount of hydrogen (~12.03 wppm) can be detected by TDS measurement in comparison with that of the as-cast specimen (~9.26 wppm). The finer microstructure and the higher density of boundaries are concluded as contributing to the hydrogen uptake in the AM specimen.
5. Based on the FEA results, the hydrogen diffusion in the studied eutectic HEA (both AM and as-cast states) is not homogenous and is highly dependent on the local microstructure. A locally higher hydrogen concentration can be expected at the PBs between the FCC/$L1_2$ and BCC/B2 phases, and thus can be responsible for the interfacial cracking of the H-charged specimens.
6. The relative orientation between the PB and the loading direction is found to contribute to the cracking susceptibility. A crack is more easily initiated from the PB when the PB is closer to be perpendicular to the loading direction. When the PB is parallel to the loading direction, the crack has a high possibility to initiate from the BCC/B2 phase.
7. A K-S-type OR is recognized in the PBs of the studied eutectic HEA, which can provide a chance for slip transfer between the two phases. Based on the EBSD analysis of the H-induced surface cracks in the AM

specimen, the normal HAGBs are shown to be more susceptible to cracking than LAGBs and PBs.

CRediT authorship contribution statement

Di Wan: Conceptualization, Methodology, Formal analysis, Investigation, Data curation, Writing – original draft, Writing – review & editing. **Shuai Guan**: Resources, Writing – original draft, Writing – review & editing. **Dong Wang**: Investigation, Writing – review & editing. **Xu Lu**: Validation, Writing – review & editing. **Jun Ma**: Formal analysis, Validation, Writing – original draft, Writing – review & editing.

Declaration of Competing Interest

The authors declare that they have no known competing financial interests or personal relationships that could have appeared to influence the work reported in this paper.

Data Availability

The raw/processed data required to reproduce these findings cannot be shared at this time as the data also forms part of an ongoing study.

Acknowledgement

The authors would like to thank the support from Department of Mechanical and Industrial Engineering (MTP), Norwegian University of Science and Technology (NTNU). The support provided by Research Council of Norway through the HyLINE (294739) and M-HEAT (294689) projects is sincerely acknowledged. In addition, the authors would like to thank Mr. J. Zhang from Northwestern Polytechnical University for the help in the FE modelling section.

Appendix A. Supporting information

Supplementary data associated with this article can be found in the online version at doi:10.1016/j.corsci.2021.110007.

References

[1] J.W. Yeh, S.K. Chen, S.J. Lin, J.Y. Gan, T.S. Chin, T.T. Shun, C.H. Tsau, S.Y. Chang, Nanostructured high-entropy alloys with multiple principal elements: novel alloy design concepts and outcomes, Adv. Eng. Mater. 6 (5) (2004) 299–303, https://doi.org/10.1002/adem.200300567.

[2] B. Gludovatz, A. Hohenwarter, D. Catoor, E.H. Chang, E.P. George, R.O. Ritchie, A fracture-resistant high-entropy alloy for cryogenic applications, Science 345 (6201) (2014) 1153–1158, https://doi.org/10.1126/science.1254581.

[3] O.N. Senkov, D.B. Miracle, K.J. Chaput, J.-P. Couzinie, Development and exploration of refractory high entropy alloys-a review, J. Mater. Res. 33 (19) (2018) 3092–3128, https://doi.org/10.1557/jmr.2018.153.

[4] Y. Qiu, S. Thomas, M.A. Gibson, H.L. Fraser, N. Birbilis, Corrosion of high entropy alloys, npj Mater. Degrad. 1 (1) (2017) 15, https://doi.org/10.1038/s41529-017-0009-y.

[5] G. Laplanche, A. Kostka, O.M. Horst, G. Eggeler, E.P. George, Microstructure evolution and critical stress for twinning in the CrMnFeCoNi high-entropy alloy, Acta Mater. 118 (2016) 152–163, https://doi.org/10.1016/j.actamat.2016.07.038.

[6] N.N. Guo, L. Wang, L.S. Luo, X.Z. Li, Y.Q. Su, J.J. Guo, H.Z. Fu, Microstructure and mechanical properties of refractory MoNbHfZrTi high-entropy alloy, Mater. Des. 81 (2015) 87–94, https://doi.org/10.1016/j.matdes.2015.05.019.

[7] O.N. Senkov, J.M. Scott, S.V. Senkova, D.B. Miracle, C.F. Woodward, Microstructure and room temperature properties of a high-entropy TaNbHfZrTi alloy, J. Alloy. Compd. 509 (20) (2011) 6043–6048, https://doi.org/10.1016/j.jallcom.2011.02.171.

[8] A. Takeuchi, K. Amiya, T. Wada, K. Yubuta, W. Zhang, High-entropy alloys with a hexagonal close-packed structure designed by equi-atomic alloy strategy and binary phase diagrams, JOM 66 (10) (2014) 1984–1992, https://doi.org/10.1007/s11837-014-1085-x.

[9] Z. Wu, H. Bei, G.M. Pharr, E.P. George, Temperature dependence of the mechanical properties of equiatomic solid solution alloys with face-centered cubic crystal structures, Acta Mater. 81 (2014) 428–441, https://doi.org/10.1016/j.actamat.2014.08.026.

[10] O.N. Senkov, G.B. Wilks, J.M. Scott, D.B. Miracle, Mechanical properties of $Nb_{25}Mo_{25}Ta_{25}W_{25}$ and $V_{20}Nb_{20}Mo_{20}Ta_{20}W_{20}$ refractory high entropy alloys, Intermetallics 19 (5) (2011) 698–706, https://doi.org/10.1016/j.intermet.2011.01.004.

[11] Y. Lu, H. Jiang, S. Guo, T. Wang, Z. Cao, T. Li, A new strategy to design eutectic high-entropy alloys using mixing enthalpy, Intermetallics 91 (2017) 124–128, https://doi.org/10.1016/j.intermet.2017.09.001.

[12] Y.P. Lu, X.Z. Gao, L. Jiang, Z.N. Chen, T.M. Wang, J.C. Jie, H.J. Kang, Y.B. Zhang, S. Guo, H.H. Ruan, Y.H. Zhao, Z.Q. Cao, T.J. Li, Directly cast bulk eutectic and near-eutectic high entropy alloys with balanced strength and ductility in a wide temperature range, Acta Mater. 124 (2017) 143–150, https://doi.org/10.1016/j.actamat.2016.11.016.

[13] I.S. Wani, T. Bhattacharjee, S. Sheikh, Y.P. Lu, S. Chatterjee, P.P. Bhattacharjee, S. Guo, N. Tsuji, Ultrafine-grained $AlCoCrFeNi_{2.1}$ eutectic high-entropy alloy, Mater. Res. Lett. 4 (3) (2016) 174–179, https://doi.org/10.1080/21663831.2016.1160451.

[14] Y. Dong, X. Gao, Y. Lu, T. Wang, T. Li, A multi-component AlCrFe2Ni2 alloy with excellent mechanical properties, Mater. Lett. 169 (2016) 62–64, https://doi.org/10.1016/j.matlet.2016.01.096.

[15] L. Jiang, Y. Lu, W. Wu, Z. Cao, T. Li, Microstructure and mechanical properties of a CoFeNi2V0.5Nb0.75 eutectic high entropy alloy in as-cast and heat-treated conditions, J. Mater. Sci. Technol. 32 (3) (2016) 245–250, https://doi.org/10.1016/j.jmst.2015.08.006.

[16] S.G. Ma, Z.M. Jiao, J.W. Qiao, H.J. Yang, Y. Zhang, Z.H. Wang, Strain rate effects on the dynamic mechanical properties of the AlCrCuFeNi2 high-entropy alloy, Mater. Sci. Eng. A 649 (2016) 35–38, https://doi.org/10.1016/j.msea.2015.09.089.

[17] X.Z. Gao, Y.P. Lu, B. Zhang, N.N. Liang, G.Z. Wu, G. Sha, J.Z. Liu, Y.H. Zhao, Microstructural origins of high strength and high ductility in an $AlCoCrFeNi_{2.1}$ eutectic high-entropy alloy, Acta Mater. 141 (2017) 59–66, https://doi.org/10.1016/j.actamat.2017.07.041.

[18] P.J. Shi, W.L. Ren, T.X. Zheng, Z.M. Ren, X.L. Hou, J.C. Peng, P.F. Hu, Y.F. Gao, Y. B. Zhong, P.K. Liaw, Enhanced strength-ductility synergy in ultrafine-grained eutectic high-entropy alloys by inheriting microstructural lamellae, Nat. Commun. 10 (2019) 489, https://doi.org/10.1038/s41467-019-08460-2.

[19] S. Chen, Y. Tong, P.K. Liaw, Additive manufacturing of high-entropy alloys: a review, Entropy 20 (12) (2018), https://doi.org/10.3390/e20120937.

[20] Y.M. Wang, T. Voisin, J.T. McKeown, J.C. Ye, N.P. Calta, Z. Li, Z. Zeng, Y. Zhang, W. Chen, T.T. Roehling, R.T. Ott, M.K. Santala, P.J. Depond, M.J. Matthews, A. V. Hamza, T. Zhu, Additively manufactured hierarchical stainless steels with high strength and ductility, Nat. Mater. 17 (1) (2018) 63–71, https://doi.org/10.1038/nmat5021.

[21] P. Kürnsteiner, M.B. Wilms, A. Weisheit, B. Gault, E.A. Jägle, D. Raabe, High-strength Damascus steel by additive manufacturing, Nature 582 (7813) (2020) 515–519, https://doi.org/10.1038/s41586-020-2409-3.

[22] Z.G. Zhu, Q.B. Nguyen, F.L. Ng, X.H. An, X.Z. Liao, P.K. Liaw, S.M.L. Nai, J. Wei, Hierarchical microstructure and strengthening mechanisms of a CoCrFeNiMn high entropy alloy additively manufactured by selective laser melting, Scr. Mater. 154 (2018) 20–24, https://doi.org/10.1016/j.scriptamat.2018.05.015.

[23] S. Guan, D. Wan, K. Solberg, F. Berto, T. Welo, T.M. Yue, K.C. Chan, Additive manufacturing of fine-grained and dislocation-populated CrMnFeCoNi high entropy alloy by laser engineered net shaping, Mater. Sci. Eng. A 761 (2019), 138056, https://doi.org/10.1016/j.msea.2019.138056.

[24] Y. Brif, M. Thomas, I. Todd, The use of high-entropy alloys in additive manufacturing, Scr. Mater. 99 (2015) 93–96, https://doi.org/10.1016/j.scriptamat.2014.11.037.

[25] I. Kunce, M. Polanski, K. Karczewski, T. Plocinski, K.J. Kurzydlowski, Microstructural characterisation of high-entropy alloy AlCoCrFeNi fabricated by laser engineered net shaping, J. Alloy. Compd. 648 (2015) 751–758, https://doi.org/10.1016/j.jallcom.2015.05.144.

[26] H. Shiratori, T. Fujieda, K. Yamanaka, Y. Koizumi, K. Kuwabara, T. Kato, A. Chiba, Relationship between the microstructure and mechanical properties of an equiatomic AlCoCrFeNi high-entropy alloy fabricated by selective electron beam melting, Mater. Sci. Eng. A 656 (2016) 39–46, https://doi.org/10.1016/j.msea.2016.01.019.

[27] S. Guan, K. Solberg, D. Wan, F. Berto, T. Welo, T.M. Yue, K.C. Chan, Formation of fully equiaxed grain microstructure in additively manufactured AlCoCrFeNiTi0.5 high entropy alloy, Mater. Des. 184 (2019), 108202, https://doi.org/10.1016/j.matdes.2019.108202.

[28] T. Borkar, B. Gwalani, D. Choudhuri, C.V. Mikler, C.J. Yannetta, X. Chen, R. V. Ramanujan, M.J. Styles, M.A. Gibson, R. Banerjee, A combinatorial assessment of $AlxCrCuFeNi2$ ($0 < x < 1.5$) complex concentrated alloys: Microstructure, microhardness, and magnetic properties, Acta Mater. 116 (2016) 63–76, https://doi.org/10.1016/j.actamat.2016.06.025.

[29] B. Gwalani, V. Soni, O.A. Waseem, S.A. Mantri, R. Banerjee, Laser additive manufacturing of compositionally graded AlCrFeMoVx ($x = 0$ to 1) high-entropy alloy system, Opt. Laser Technol. 113 (2019) 330–337, https://doi.org/10.1016/j.optlastec.2019.01.009.

[30] S. Guan, D. Wan, K. Solberg, F. Berto, T. Welo, T.M. Yue, K.C. Chan, Additively manufactured CrMnFeCoNi/AlCoCrFeNiTi0.5 laminated high-entropy alloy with enhanced strength-plasticity synergy, Scr. Mater. 183 (2020) 133–138, https://doi.org/10.1016/j.scriptamat.2020.03.032.

[31] W.H. Johnson, On Some Remarkable Changes Produced in Iron and Steel by the Action of Hydrogen and Acids, Proceedings of the Royal Society of London 23 (156–163) (1875) 168–179, doi: 10.1098/rspl.1874.0024.

[32] B.H. Sun, D. Wang, X. Lu, D. Wan, D. Ponge, X.C. Zhang, Current Challenges and opportunities toward understanding hydrogen embrittlement mechanisms in

advanced high-strength steels: a review, Acta Metall. Sin. Engl. Lett. 34 (6) (2021) 741–754, https://doi.org/10.1007/s40195-021-01233-1.
[33] H.K. Birnbaum, P. Sofronis, Hydrogen-enhanced localized plasticity—a mechanism for hydrogen-related fracture, Mater. Sci. Eng. A 176 (1–2) (1994) 191–202, https://doi.org/10.1016/0921-5093(94)90975-x.
[34] I.M. Robertson, The effect of hydrogen on dislocation dynamics, Eng. Fract. Mech. 68 (6) (2001) 671–692, https://doi.org/10.1016/S0013-7944(01)00011-X.
[35] S. Wang, A. Nagao, P. Sofronis, I.M. Robertson, Hydrogen-modified dislocation structures in a cyclically deformed ferritic-pearlitic low carbon steel, Acta Mater. 144 (2018) 164–176, https://doi.org/10.1016/j.actamat.2017.10.034.
[36] R.A. Oriani, P.H. Josephic, Equilibrium and kinetic studies of the hydrogen-assisted cracking of steel, Acta Met. 25 (9) (1977) 979–988, https://doi.org/10.1016/0001-6160(77)90126-2.
[37] K. Takai, H. Shoda, H. Suzuki, M. Nagumo, Lattice defects dominating hydrogen-related failure of metals, Acta Mater. 56 (18) (2008) 5158–5167, https://doi.org/10.1016/j.actamat.2008.06.031.
[38] S.P. Lynch, Environmentally assisted cracking - overview of evidence for an adsorption-induced localized-slip process, Acta Met. 36 (10) (1988) 2639–2661, https://doi.org/10.1016/0001-6160(88)90113-7.
[39] S.P. Lynch, Comments on "A unified model of environment-assisted cracking", Scr. Mater. 61 (3) (2009) 331–334, https://doi.org/10.1016/j.scriptamat.2009.02.031.
[40] R. Kirchheim, Revisiting hydrogen embrittlement models and hydrogen-induced homogeneous nucleation of dislocations, Scr. Mater. 62 (2) (2010) 67–70, https://doi.org/10.1016/j.scriptamat.2009.09.037.
[41] M.B. Djukic, G.M. Bakic, V.S. Zeravcic, A. Sedmak, B. Rajicic, Hydrogen embrittlement of industrial components: prediction, prevention, and models, Corrosion 72 (7) (2016) 943–961, https://doi.org/10.5006/1958.
[42] M.B. Djukic, G.M. Bakic, V. Sijacki Zeravcic, A. Sedmak, B. Rajicic, The synergistic action and interplay of hydrogen embrittlement mechanisms in steels and iron: Localized plasticity and decohesion, Eng. Fract. Mech. 216 (2019), 106528, https://doi.org/10.1016/j.engfracmech.2019.106528.
[43] A. Barnoush, Hydrogen embrittlement, revisited by in situ electrochemical nanoindentation, Mater. und Werkst., Univ. Des. Saarl., Aachen (2009) 256.
[44] K. Ichii, M. Koyama, C.C. Tasan, K. Tsuzaki, Comparative study of hydrogen embrittlement in stable and metastable high-entropy alloys, Scr. Mater. 150 (2018) 74–77, https://doi.org/10.1016/j.scriptamat.2018.03.003.
[45] H. Luo, Z. Li, W. Lu, D. Ponge, D. Raabe, Hydrogen embrittlement of an interstitial equimolar high-entropy alloy, Corros. Sci. 136 (2018) 403–408, https://doi.org/10.1016/j.corsci.2018.03.040.
[46] Z. Pu, Y. Chen, L.H. Dai, Strong resistance to hydrogen embrittlement of high-entropy alloy, Mater. Sci. Eng. A 736 (2018) 156–166, https://doi.org/10.1016/j.msea.2018.08.101.
[47] C. Zhang, Y. Wu, L. You, W. Qiu, Y. Zhang, Y. Yuan, Z. Lu, X. Song, Nanoscale phase separation of TiZrNbTa high entropy alloy induced by hydrogen absorption, Scr. Mater. 178 (2020) 503–507, https://doi.org/10.1016/j.scriptamat.2019.12.034.
[48] Y. Lu, X. Gao, L. Jiang, Z. Chen, T. Wang, J. Jie, H. Kang, Y. Zhang, S. Guo, H. Ruan, Y. Zhao, Z. Cao, T. Li, Directly cast bulk eutectic and near-eutectic high entropy alloys with balanced strength and ductility in a wide temperature range, Acta Mater. 124 (2017) 143–150, https://doi.org/10.1016/j.actamat.2016.11.016.
[49] P. Shi, W. Ren, T. Zheng, Z. Ren, X. Hou, J. Peng, P. Hu, Y. Gao, Y. Zhong, P. K. Liaw, Enhanced strength-ductility synergy in ultrafine-grained eutectic high-entropy alloys by inheriting microstructural lamellae, Nat. Commun. 10 (1) (2019) 489, https://doi.org/10.1038/s41467-019-08460-2.
[50] I.S. Wani, T. Bhattacharjee, S. Sheikh, P.P. Bhattacharjee, S. Guo, N. Tsuji, Tailoring nanostructures and mechanical properties of AlCoCrFeNi2.1 eutectic high entropy alloy using thermo-mechanical processing, Mater. Sci. Eng. A 675 (2016) 99–109, https://doi.org/10.1016/j.msea.2016.08.048.
[51] Y. Zhang, J. Li, X. Wang, Y. Lu, Y. Zhou, X. Sun, The interaction and migration of deformation twin in an eutectic high-entropy alloy AlCoCrFeNi2.1, J. Mater. Sci. Technol. 35 (5) (2019) 902–906, https://doi.org/10.1016/j.jmst.2018.09.067.
[52] D. Wan, A. Barnoush, Plasticity in cryogenic brittle fracture of ferritic steels: dislocation versus twinning, Mater. Sci. Eng., A 744 (2019) 335–339, https://doi.org/10.1016/j.msea.2018.12.038.
[53] G. Hachet, A. Oudriss, A. Barnoush, R. Milet, D. Wan, A. Metsue, X. Feaugas, The influence of hydrogen on cyclic plasticity of <001> oriented nickel single crystal. Part I: Dislocation organisations and internal stresses, Int. J. Plast. 126 (2020), https://doi.org/10.1016/j.ijplas.2019.09.017.
[54] X. Lu, D. Wang, D. Wan, Z.B. Zhang, N. Kheradmand, A. Barnoush, Effect of electrochemical charging on the hydrogen embrittlement susceptibility of alloy 718, Acta Mater. 179 (2019) 36–48, https://doi.org/10.1016/j.actamat.2019.08.020.
[55] D. Wang, X. Lu, D. Wan, X. Guo, R. Johnsen, Effect of hydrogen on the embrittlement susceptibility of Fe–22Mn-0.6C TWIP steel revealed by in-situ tensile tests, Mater. Sci. Eng., A 802 (2021), 140638, https://doi.org/10.1016/j.msea.2020.140638.
[56] D. Wang, X. Lu, Y. Deng, D. Wan, Z. Li, A. Barnoush, Effect of hydrogen-induced surface steps on the nanomechanical behavior of a CoCrFeMnNi high-entropy alloy revealed by in-situ electrochemical nanoindentation, Intermetallics 114 (2019), 106605, https://doi.org/10.1016/j.intermet.2019.106605.
[57] D. Wang, X. Lu, D. Wan, Z. Li, A. Barnoush, In-situ observation of martensitic transformation in an interstitial metastable high-entropy alloy during cathodic hydrogen charging, Scr. Mater. 173 (2019) 56–60, https://doi.org/10.1016/j.scriptamat.2019.07.042.
[58] S. Zaefferer, N.N. Elhami, Theory and application of electron channelling contrast imaging under controlled diffraction conditions, Acta Mater. 75 (2014) 20–50, https://doi.org/10.1016/j.actamat.2014.04.018.
[59] Y. Xiong, W.H. Hofmeister, Z. Cheng, J.E. Smugeresky, E.J. Lavernia, J. M. Schoenung, In situ thermal imaging and three-dimensional finite element modeling of tungsten carbide–cobalt during laser deposition, Acta Mater. 57 (18) (2009) 5419–5429, https://doi.org/10.1016/j.actamat.2009.07.038.
[60] H. Yin, S.D. Felicelli, Dendrite growth simulation during solidification in the LENS process, Acta Mater. 58 (4) (2010) 1455–1465, https://doi.org/10.1016/j.actamat.2009.10.053.
[61] T. Depover, K. Verbeken, The effect of TiC on the hydrogen induced ductility loss and trapping behavior of Fe-C-Ti alloys, Corros. Sci. 112 (2016) 308–326, https://doi.org/10.1016/j.corsci.2016.07.013.
[62] X. Chen, W.W. Gerberich, The kinetics and micromechanics of hydrogen assisted cracking in Fe-3 pct Si single crystals, Metall. Trans. A 22 (1) (2012) 59–70, https://doi.org/10.1007/bf03350949.
[63] D. Wang, X. Lu, Y. Deng, X. Guo, A. Barnoush, Effect of hydrogen on nanomechanical properties in Fe-22Mn-0.6C TWIP steel revealed by in-situ electrochemical nanoindentation, Acta Mater. 166 (2019) 618–629, https://doi.org/10.1016/j.actamat.2018.12.055.
[64] A. Turk, S. Pu, D. Bombač, P.E.J. Rivera-Díaz-del-Castillo, E.I. Galindo-Nava, Quantification of hydrogen trapping in multiphase steels: part II – effect of austenite morphology, Acta Mater. 197 (2020) 253–268, https://doi.org/10.1016/j.actamat.2020.07.039.
[65] P. Tao, J. Gong, Y. Wang, W. Cen, J. Zhao, Modeling of hydrogen diffusion in duplex stainless steel based on microstructure using finite element method, Int. J. Press. Vessel. Pip. 180 (2020), 104031, https://doi.org/10.1016/j.ijpvp.2019.104031.
[66] T. Bhattacharjee, I.S. Wani, S. Sheikh, I.T. Clark, T. Okawa, S. Guo, P. P. Bhattacharjee, N. Tsuji, Simultaneous Strength-ductility enhancement of a nano-lamellar AlCoCrFeNi2.1 eutectic high entropy alloy by cryo-rolling and annealing, Sci. Rep. 8 (1) (2018) 3276, https://doi.org/10.1038/s41598-018-21385-y.
[67] S.R. Reddy, S. Yoshida, T. Bhattacharjee, N. Sake, A. Lozinko, S. Guo, P. P. Bhattacharjee, N. Tsuji, Nanostructuring with structural-compositional dual heterogeneities enhances strength-ductility synergy in eutectic high entropy alloy, Sci. Rep. 9 (1) (2019) 11505, https://doi.org/10.1038/s41598-019-47983-y.
[68] X. Gao, Y. Lu, B. Zhang, N. Liang, G. Wu, G. Sha, J. Liu, Y. Zhao, Microstructural origins of high strength and high ductility in an AlCoCrFeNi2.1 eutectic high-entropy alloy, Acta Mater. 141 (2017) 59–66, https://doi.org/10.1016/j.actamat.2017.07.041.
[69] J. Campbell, Cavitation During Superplastic Forming, Materials 4 (7) (2011) 1271–1286, https://doi.org/10.3390/ma4071271.
[70] Y. Zhu, S. Zhou, Z. Xiong, Y.-J. Liang, Y. Xue, L. Wang, Enabling stronger eutectic high-entropy alloys with larger ductility by 3D printed directional lamellae, Addit. Manuf. 39 (2021), 101901, https://doi.org/10.1016/j.addma.2021.101901.
[71] Z. Hua, S. Zhu, B. An, T. Iijima, C. Gu, J. Zheng, The finding of hydrogen trapping at phase boundary in austenitic stainless steel by scanning Kelvin probe force microscopy, Scr. Mater. 162 (2019) 219–222, https://doi.org/10.1016/j.scriptamat.2018.11.020.
[72] D. Wan, Y. Ma, B. Sun, S.M.J. Razavi, D. Wang, X. Lu, W. Song, Evaluation of hydrogen effect on the fatigue crack growth behavior of medium-Mn steels via in-situ hydrogen plasma charging in an environmental scanning electron microscope, J. Mater. Sci. Technol. 85 (2021) 30–43, https://doi.org/10.1016/j.jmst.2020.12.069.
[73] A. Oudriss, J. Creus, J. Bouhattate, E. Conforto, C. Berziou, C. Savall, X. Feaugas, Grain size and grain-boundary effects on diffusion and trapping of hydrogen in pure nickel, Acta Mater. 60 (19) (2012) 6814–6828, https://doi.org/10.1016/j.actamat.2012.09.004.
[74] A. Rohsler, O. Sobol, H. Hanninen, T. Bollinghaus, In-situ ToF-SIMS analyses of deuterium re-distribution in austenitic steel AISI 304L under mechanical load, Sci. Rep. 10 (1) (2020) 3611, https://doi.org/10.1038/s41598-020-60370-2.
[75] A. Nagao, M. Dadfarnia, B.P. Somerday, P. Sofronis, R.O. Ritchie, Hydrogen-enhanced-plasticity mediated decohesion for hydrogen-induced intergranular and "quasi-cleavage" fracture of lath martensitic steels, J. Mech. Phys. Solids 112 (2018) 403–430, https://doi.org/10.1016/j.jmps.2017.12.016.
[76] P. Novak, R. Yuan, B.P. Somerday, P. Sofronis, R.O. Ritchie, A statistical, physical-based, micro-mechanical model of hydrogen-induced intergranular fracture in steel, J. Mech. Phys. Solids 58 (2) (2010) 206–226, https://doi.org/10.1016/j.jmps.2009.10.005.
[77] B.N. Popov, J.-W. Lee, M.B. Djukic, Hydrogen permeation and hydrogen-induced cracking, Handb. Environ. Degrad. Mater. (2018) 133–162.
[78] Z. Hua, B. An, T. Iijima, C. Gu, J. Zheng, The finding of crystallographic orientation dependence of hydrogen diffusion in austenitic stainless steel by scanning Kelvin probe force microscopy, Scr. Mater. 131 (2017) 47–50, https://doi.org/10.1016/j.scriptamat.2017.01.003.
[79] Q. Wang, Y. Lu, Q. Yu, Z. Zhang, The exceptional strong face-centered cubic phase and semi-coherent phase boundary in a eutectic dual-phase high entropy alloy AlCoCrFeNi, Sci. Rep. 8 (1) (2018) 14910, https://doi.org/10.1038/s41598-018-33330-0.
[80] K. Nibur, D. Bahr, B. Somerday, Hydrogen effects on dislocation activity in austenitic stainless steel, Acta Mater. 54 (10) (2006) 2677–2684, https://doi.org/10.1016/j.actamat.2006.02.007.

[81] D. Kuhlmann-Wilsdorf, Theory of plastic deformation: - properties of low energy dislocation structures, Mater. Sci. Eng. A 113 (1989) 1–41, https://doi.org/10.1016/0921-5093(89)90290-6.
[82] P. Shi, R. Li, Y. Li, Y. Wen, Y. Zhong, W. Ren, Z. Shen, T. Zheng, J. Peng, X. Liang, P. Hu, N. Min, Y. Zhang, Y. Ren, P.K. Liaw, D. Raabe, Y.-D. Wang, Hierarchical crack buffering triples ductility in eutectic herringbone high-entropy alloys, Science 373 (6557) (2021) 912–918, https://doi.org/10.1126/science.abf6986.
[83] B. Sun, W. Lu, B. Gault, R. Ding, S.K. Makineni, D. Wan, C.H. Wu, H. Chen, D. Ponge, D. Raabe, Chemical heterogeneity enhances hydrogen resistance in high-strength steels, Nat. Mater. 20 (2021) 1629–1634, https://doi.org/10.1038/s41563-021-01050-y.